CHAPTER 6

THE EINSTEIN CROSS: LENSING VS. STELLAR DYNAMICS

ABSTRACT

We study the total mass distribution in the inner parts of the lens galaxy in the Einstein Cross by combining gravitational lensing with stellar dynamics. We obtain a realistic luminosity density of the lens galaxy by deprojecting its observed surface brightness, and we construct a lens model that accurately fits the positions and relative fluxes of the four quasar images. We combine both to build axisymmetric dynamical models that fit preliminary two-dimensional stellar kinematics derived from recent observations with the integral-field spectrograph GMOS. We find that the stellar velocity dispersion measurements with a mean value of $167 \pm 10\,\mathrm{km\,s^{-1}}$ within the Einstein radius $R_E = 0.90''$, are in agreement with predictions from our and previous lens models. From the best-fit dynamical model, with I-band mass-to-light ratio $M/L = 3.6\,\mathrm{M_\odot/L_\odot}$, the Einstein mass is consistent with $M_E = 1.60 \times 10^{10}\,\mathrm{M_\odot}$ from our lens model. The shapes of the density inferred from the lens model and from the surface brightness are very similar, but further improvement on the preliminary kinematic data is needed, before firm conclusions on the total mass distribution can be drawn.

1 INTRODUCTION

IN the cold dark matter (CDM) paradigm for galaxy formation (e.g., Kauffmann & van den Bosch 2002), galaxies are embedded in extended dark matter distributions with a specific and universal shape. Although we cannot directly see this dark matter, it contributes to the gravitational potential and hence it influences the dynamics of the galaxy. Measurements of rotation curves from neutral Hydrogen (H I) observations in the outer parts of late-type galaxies have provided evidence for the presence of dark matter in these systems more than two decades ago (e.g., van Albada et al. 1985). In the outer parts of early-type galaxies, however, cold gas is scarce, and evidence for dark matter in these systems has been found (mainly) from stellar kinematics (e.g., Carollo et al. 1995; Gerhard et al. 2001; but see Romanowsky et al. 2003).

A fundamental problem in using stellar kinematics for this purpose is the mass-anisotropy degeneracy: a change in the measured line-of-sight velocity dispersion can be due to a change in mass, but also due to a change in velocity anisotropy. Both effects can be disentangled by measuring also the higher-order velocity moments (Dejonghe 1988; van der Marel & Franx 1993; Gerhard 1993), but only the inner parts of nearby galaxies are bright enough to obtain the required kinematic measurements. Fitting dynamical models to such observations has provided accurate measurements of the anisotropy and M/L in the inner parts of early-type galaxies (e.g., van der Marel et al. 1991; Rix et al. 1997; Gerhard et al. 2001; Cappellari et al. 2005).

The dark matter fraction can be estimated by comparing this total (luminous and dark) M/L with the stellar (luminous) $M_\star/L$ determined by fitting stellar population models to color and absorption line-strength measurements. Due to uncertainties in the stellar population models (particularly with respect to the initial mass function), however, the dark matter fraction is not well constrained in this way.

The central dark matter profile provides a critical test of the CDM paradigm, which predicts that the inner parts of galaxies have a cuspy density $\propto r^{-\gamma}$, with power-law slope $\gamma \sim 1$ (Navarro, Frenk & White 1997). However, the observed slopes from H I rotation curves of late-type galaxies are on average much shallower, and even less is known about this apparent 'cusp/core-problem' in early-type galaxies (see e.g. Primack 2004 for an overview). Due to this lack of constraint, the dark matter profile in the inner parts of early-type galaxies is often restricted to the assumption that mass follows light, i.e., constant M/L.

A unique method to address the above issues is via the use of strong gravitational lensing. In combination with stellar dynamics, strong gravitational lensing can simultaneously break the mass-anisotropy degeneracy, and determine the fraction and shape of the dark matter distribution. The mass of a foreground galaxy bends the light of a distant bright object behind it, resulting in multiple images. From the separation and fluxes of the images the total mass distribution of the lens galaxy can be inferred. The luminous distribution can be obtained from the surface brightness of the lens galaxy, and dynamical models can then be constructed. Fitting the kinematics predicted by these models to the observed stellar kinematics places constraints on the free parameters, including anisotropy, stellar $M_\star/L$ and central dark matter slope γ.

Treu & Koopmans (2004, and references therein) have applied this approach to several lensing systems, of which 0047-281 (Koopmans & Treu 2003) is the best constrained case, with three spatially-resolved velocity dispersion measurements extending to about the effective radius of the lens galaxy. They measured the total mass

within the Einstein radius by fitting a singular isothermal ellipsoid to the positions of the quasar images. This total mass is then used to constrain the relative contribution to the potential from a luminous and dark matter component, both of which they assume to be a simple spherical distribution. They then compared the dispersions predicted by the spherical Jeans equations, for an ad-hoc assumption of the velocity anisotropy, with the observed dispersions. Based on a well constrained $M_\star/L$ and an upper limit on γ, they conclude that a significant amount of dark matter is present in the inner parts of the lens galaxy, with a slope flatter than the light. However, their results are limited by too few kinematic constraints (which leaves the anisotropy degenerate), and by the use of a simple spherical dynamical model.

The use of non-spherical models is important, since triaxial dark matter distributions are predicted by the CDM paradigm (e.g., Jing & Suto 2002). A triaxial geometry also seems necessary to explain the lens statistics (e.g., Oguri & Keeton 2004). Above all, most lens galaxies are significantly flattened and so cannot be well-described by spherical models. Non-spherical models provide a more realistic description of the lens galaxy, but the increase in freedom requires also (significantly) more spatially resolved kinematic measurements to constrain them. Only very few of the known strong gravitational lens systems are close enough to obtain such kinematic data, e.g., via observations with integral-field spectrographs. One of them is the gravitational lens system QSO 2237+0305, well-known as the Einstein Cross, with the lens galaxy at a redshift $z_{\rm lens} \sim 0.04$. We have observed the Einstein Cross with the integral-field spectrograph GMOS on the Gemini-North Telescope. We combine a detailed model of the gravitational lens system with the light distribution inferred directly from the surface brightness to construct realistic non-spherical dynamical models. We then fit these models to the two-dimensional GMOS kinematics to investigate the mass distribution in the inner parts of the lens galaxy, including a possible contribution from dark matter.

In Section 2 we briefly describe the Einstein Cross and we present the photometric and kinematic observations we use in Section 3 to construct a detailed lens and dynamical model. In Section 4 we present our results. We discuss our findings in Section 5 and summarize our conclusions in Section 6. We adopt the WMAP cosmological parameters for the Hubble constant, the matter density and the cosmological constant, of $H_0 = 71\,{\rm km\,s^{-1}\,Mpc^{-1}}$, $\Omega_M = 0.27$ and $\Omega_L = 0.73$, respectively (Bennett et al. 2003), although these parameters only have a small effect on the physical scales of the lens galaxy due to its proximity.

2 OBSERVATIONS

2.1 THE EINSTEIN CROSS

The Einstein Cross is the well-known gravitational lens system QSO 2237+0305 or PGC069457 ($22^h40^m30.3^s$, $+03^\circ\,21'31''$). In this system, a distant quasar at $z_{\rm source} = 1.695$ is lensed by the bulge of an early-type spiral at $z_{\rm lens} = 0.0394$, resulting in a cross of four bright images separated by about $1.8''$.

Because the Einstein Cross has long been the closest strong gravitational lens system known, it has been very well studied since its discovery by Huchra et al. (1985). There is a wealth of ground- and space-based imaging data at all wavelengths (e.g., Falco et al. 1996; Blanton, Turner & Wambsganss 1998; Agol, Jones & Blaes 2000; Dai et al. 2003). The resulting precise measurements of the positions and relative fluxes of the quasar images can be used to construct a detailed lens model.

In contrast, kinematic data of the lens galaxy is very scarce, with only one measured central stellar velocity dispersion (Foltz et al. 1992) and two H I rotation curve measurements in the very outer parts (Barnes et al. 1999). There are several previous integral-field studies of the Einstein Cross (TIGER: Fitte & Adam 1994; INTEGRAL: Mediavilla et al. 1998; CIRPASS: Metcalf et al. 2004). However, none of these studies were concerned with the the stellar kinematics of the lens galaxy, but instead investigated the quasar spectra.

2.2 IMAGING

Strong gravitational lensing occurs when a bright distant source like a quasar is sufficiently aligned with a foreground massive object such as an early-type elliptical galaxy. The lens galaxy then bends and magnifies the light from the quasar into separate images. The more precise the positions and relative fluxes of the quasar images are measured, the better the total (projected) mass distribution of the lens galaxy is constrained. Here, we use the accurate positions from the website of the CASTLES survey[1] based on *Hubble Space Telescope* (HST) imaging. Although optical flux ratios are given on this website, we use the radio fluxes provided by Falco et al. (1996), because they are in general (much) less affected by differential extinction or microlensing.

Instead of assuming a simple functional form for the light distribution as in most previous studies, we construct in § 3.1 a density model that in projection reproduces the surface brightness in detail. We measure the inclination needed to deproject the surface brightness from the flattening of the disk in a WFPC2/F555W V-band image (Fig. 1, left panel), retrieved from the HST-archive (1600 seconds; PI: Westphal). For the actual construction of the density model we use a WFPC2/F814W I-band image (Fig. 1, right panel) from the HST-archive (120 seconds; PI: Kochanek). We correct the I-band image for extinction following Schlegel, Finkbeiner & Davis (1998), and we convert to solar units using the WFPC2 calibration of Dolphin (2000), while assuming an absolute I-band magnitude for the Sun of 4.08 mag (Table 2 of Binney & Merrifield 1998). From a de Vaucouleurs $R^{1/4}$ profile fit to the I-band photometry in the inner $3''$ bulge region, we obtain an effective radius $R_e \sim 6''$, which is consistent with previous measurements (e.g., Racine 1991).

2.3 INTEGRAL-FIELD SPECTROSCOPY

Observations of the Einstein Cross lens system were carried out using the integral-field unit of the GMOS-North spectrograph (Murray et al. 2003; Hook et al. 2004) on July 17$^{\rm th}$ and August 1$^{\rm st}$ 2005 as part of the program GN-2005A-DD-7. The data were obtained using the IFU two-slit mode that provides a field-of-view of $5''\times7''$. An array of 1500 hexagonal lenslets, of which 500 are located $1'$ away from the main field to be used for sky subtraction, sets the $0\farcs2$ spatial sampling. Eight individual exposures of 1895 seconds each were obtained during the two nights, resulting in a total on-source integration time of $\sim$4 hours. An offset of $0\farcs3$ was introduced between exposures to avoid bad CCD regions or lost fibers. The R400-G5305 grating in combination with the CaT-G0309 filter was used to cover a wavelength range between 7800-9200 Å with a spectral resolution of 2.8 Å (FWHM).

[1] http://cfa-www.harvard.edu/castles/

To perform the data reduction we use an updated version of the officially distributed Gemini IRAF[2] package (B. Miller, priv. comm.). For each frame CuAr and Quartz Halogen (QH) lamp exposures were taken before each target for wavelength calibration and flat-fielding purposes. We bias subtract, flat-field and apply cosmic ray rejection to each science frame before the extraction of the data. An accurate flat-fielding is particularly important since at the observed wavelengths the data is affected by fringing. We minimize the effect of fringes in the final data by using the QH lamp exposures taken just before each science frame. For the cosmic ray rejection we use the *L.A. Cosmic* algorithm by van Dokkum (2001). After the extraction, we use the CuAr lamps closest to each science frame for wavelength calibration.

In order to check the range of fiber-to-fiber variations of the spectral resolution of the instrument, we measure the width of the sky lines in each fiber. As expected, the values on each fiber yield the nominal value (2.8 $\pm$ 0.2 Å). For the sky subtraction, given the small scatter in the instrumental resolution of each fiber, we generate a single sky spectrum from all the sky fibers. This exercise, however, lead to significant residuals in the sky subtracted science frames. In each science frame, the data is grouped in blocks of science fibers surrounded by sky lenses. In an attempt to minimize the residuals in the sky subtracted frame, we subtract the averaged sky lenses closer to each group of science lenses. This approach leads to a significant improvement in the final sky subtracted results. Additionally, before the merging of the individual exposures, we homogenize each science frame for the fiber-to-fiber resolution variations by convolving each individual spectrum to an instrumental resolution of 3.2 Å (FWHM). We also resample the individual exposures, so that they have the same starting value and sampling in wavelength. Before the merging process, we interpolate each individual frame to a common grid taking into account the small spatial offsets applied during the observations. We then sum the spectra sharing the same position in the sky to produce the final merged datacube.

3 ANALYSIS

We determine the intrinsic light distribution of the lens galaxy from its surface brightness, we fit a lens model to the quasar images, and we extract the stellar velocity and dispersion maps of the inner parts of the lens galaxy from the integral-field spectroscopic observations. These are then the ingredients for constructing an axisymmetric dynamical model of the lens galaxy.

3.1 LIGHT DISTRIBUTION

We construct a stellar luminosity density model of the lens galaxy based on its observed surface brightness with HST. For this we use the Multi-Gaussian Expansion (MGE) parametrization by Emsellem, Monnet & Bacon (1994), which describes the observed surface brightness as a sum of Gaussians. Even though Gaussians do not form a complete set of functions, in general the photometry is accurately reproduced, including ellipticity variations and non-elliptical isophotes. In Fig. 1 we show MGE fits to the V-band and I-band HST images, obtained with the software of Cappellari (2002), while masking the quasar images. Although the adopted constant-PA model

[2]IRAF is distributed by the National Optical Astronomy Observatories, which are operated by the Association of Universities for Research in Astronomy, Inc., under cooperative agreement with the National Science Foundation.

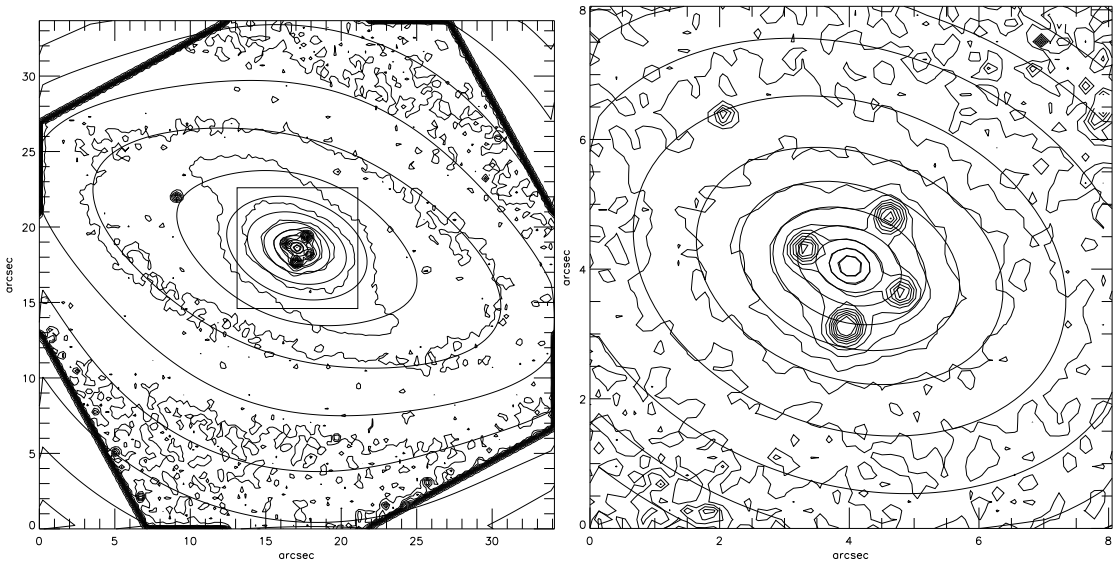

FIGURE 1 — *The surface brightness of the lens galaxy in the Einstein Cross as observed with HST. Left panel: the contours of the WFPC2/F555W V-band image reveal clearly the bulge, spiral arms and bar embedded in the large-scale disk of this early-type spiral galaxy. The ellipticity measured from the MGE fit (solid contours) is used to estimate the inclination. Right panel: the central 8″×8″of the WFPC2/F814W I-band image, of which the MGE fit (solid contours) is used to construct the stellar density model of the lens galaxy. We use the I-band image instead of the longer exposed V-band image as it tracers better the old stellar population and is less sensitive to extinction and reddening. The four quasar images are masked out during the MGE fit. The contours are in steps of 0.5 mag/arcsec^2 and the WFPC images are rotated such that North is up and East is to the left.*

cannot reproduce the bar and spiral arms, it provides a very good description of the disk in the outer parts (left panel) and reproduces well the bulge in the inner parts (right panel).

The position angle (PA) of the major axis of the MGE isophotes (with respect to North through East) is $\sim 70^\circ$. This is consistent with measurements by Yee (1988), who found PA$\sim 67^\circ$ for the axis through quasar images C and D, bracketed by PA$\sim 77^\circ$ for the outer disk and PA$\sim 39^\circ$ for the bar (see also Fig. 1 of Trott & Webster 2002).

The MGE-parametrization of the surface brightness has the advantage that the deprojection can be performed analytically once the inclination i is known (Monnet, Bacon & Emsellem 1992). From the MGE fit to the V-band surface brightness of the lens galaxy (left panel of Fig. 1), we find that Gaussian components as flat as $q' = 0.4$ are required for an acceptable fit. This sets a lower limit to the inclination of $i \gtrsim 66^\circ$, which is above the value of $i \sim 60^\circ$ found by Irwin et al. (1989). Assuming a lower limit for the *intrinsic* flattening of the disk of 0.15 (e.g., Lambas, Maddox & Loveday 1992), we obtain an inclination of $i = 68^\circ$.

Given this inclination, we deproject the I-band MGE surface brightness fit, to obtain the axisymmetric stellar luminosity density $j_\star(R, \theta)$ in the meridional plane of the lens galaxy, still expressed as a sum of Gaussians. The intrinsic flattening of the embedded bulge component is around 0.64.

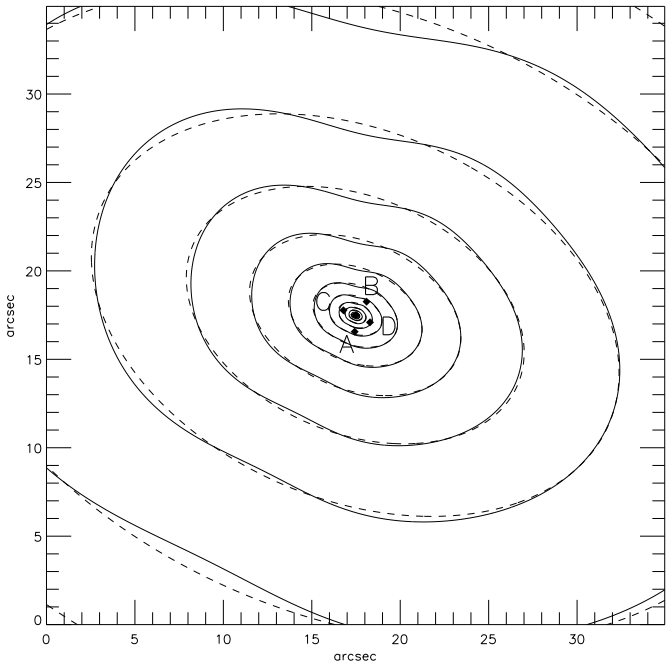

FIGURE 2 — *The surface mass density from the gravitational lens model of the Einstein Cross (solid contours). The scale-free lens model fits the positions and relative fluxes of the quasar images, indicated by the filled circles. Superposed are the (dashed) contours of an MGE fit. As in Fig. 1, the contours are in steps of 0.5 mag/arcsec^2, and North is up and East is to the left.*

3.2 LENS MODEL

We use the algorithm of Evans & Witt (2003) to construct a lens model that accurately fits the (optical) positions and relative (radio) fluxes of the four quasar images (§ 2.2) in the Einstein Cross. The (projected) potential of the lens galaxy is assumed to be a scale-free function $\Phi_{\rm lens}(R',\theta') = R'^{\beta}F(\theta')$ of the polar coordinates R' and θ' in the lens sky-plane, with $0<\beta<2$ for realistic models. The angular part $F(\theta')$ is expanded as a Fourier series

$$F(\theta') = \frac{1}{2}\,a_0 + \sum_{m=1}^{\infty}[c_m\cos(m\theta') + s_m\sin(m\theta')]. \tag{3.1}$$

We consider the models with $\beta=1$ since they are interesting in two ways. These models have an everywhere flat rotation curve, and hence are projections of axisymmetric and triaxial generalizations of the familiar isothermal sphere. Moreover, as shown by Evans & Witt (2003), the lens model that best fits the positions and relative fluxes of the quasar images follows by straightforward matrix inversion.

The positions (R'_i,θ'_i) of the images are related to the position (ξ',η') of the quasar by the lens equation (e.g., Schneider, Ehlers & Falco 1992), which for $\beta=1$ reduces to

$$\xi' = [R'_i - F(\theta'_i)]\cos\theta'_i + F'(\theta'_i)\sin\theta'_i, \tag{3.2}$$

$$\eta' = [R'_i - F(\theta'_i)]\sin\theta'_i - F'(\theta'_i)\cos\theta'_i. \tag{3.3}$$

The flux ratios of the images follow from their magnifications, for $\beta = 1$ given by

$$\mu_i = 1 - [F(\theta'_i) + F''(\theta'_i)]/R'_i. \tag{3.4}$$

Both equations are linear in the free parameters, i.e., the Fourier coefficients (c_m, s_m) and the quasar position (ξ', η'), so that the solution indeed follows by matrix inversion.

The Einstein Cross consists of four quasar images, resulting in 8 constraints from their positions and 3 from their flux ratios, so that in total we can constrain up to 11 free parameters. Although we can in principle fit the constraints exactly, we take into account the observational errors in the constraints (including for the positions the uncertainty in the measurement of the center of the lens galaxy). From the models that fit the constraints within the observational errors, we choose the solution with the smallest Fourier components higher than $m = 2$, as it looks most like a real galaxy. The resulting 11 best-fit parameters[3] are $\xi' = 0.0696$, $\eta' = -0.0133$ for the source position with respect to the center of the lens galaxy, and $c_0 = 1.7746$, $c_2 = -0.04223$, $s_2 = 0.0428$, $c_3 = 0.0004$, $s_3 = -0.0014$, $c_4 = 0.0008$, $s_4 = 0.0009$, $c_5 = -0.0001$, $s_5 = 0.0007$, all in arcseconds.

The Fourier coefficients c_1 and s_1 are set to zero as they do not contribute to the inferred surface mass density, which follows from Poisson's equation as

$$\Sigma_{\rm lens}(R', \theta') = \Sigma_{\rm crit}\, \frac{F(\theta') + F''(\theta')}{2\, R'}, \quad \text{with} \quad \Sigma_{\rm crit} = \frac{c^2\, D_s}{4\pi G\, D_l\, D_{ls}}, \tag{3.5}$$

where D_l, D_s and D_{ls} are the (angular diameter) distance to the lens galaxy, the quasar source and the distance from lens to source, respectively. The contours of $\Sigma_{\rm lens}(R', \theta')$ for the best-fit lens model of the Einstein Cross are shown in Fig. 2.

The scale-free $\beta = 1$ lens models have the further advantage that it is straightforward to compute the mass within the critical curve, which is given by

$$R_{\rm crit}(\theta') = F(\theta') + F''(\theta'), \tag{3.6}$$

with $R_{\rm crit}$ in arcseconds. From the area within this critical curve, $A_{\rm crit}$, it follows that

$$M_{\rm crit} = \Sigma_{\rm crit}\, A_{\rm crit}\, \left(D_l\, \pi/648000\right)^2, \tag{3.7}$$

where the factor in parentheses is the conversion from arcsec to pc for a given distance to the lens galaxy D_l in pc. The critical area $A_{\rm crit}$ (in arcsec^2) can also be computed directly from the Fourier coefficients (cf. eq. 31 of Evans & Witt 2003[4])

$$A_{\rm crit} = \frac{1}{4}\, a_0^2 + \frac{1}{2} \sum_{m=1}^{\infty} (m^2 - 1)^2 (c_m^2 + s_m^2). \tag{3.8}$$

The critical mass $M_{\rm crit}$ also provides a good approximation of the Einstein mass M_E within the Einstein radius R_E, which can be obtained from the critical area as $R_E = \sqrt{A_{\rm crit}/\pi}$ (in arcseconds), and describes the circle that approximately traces the positions of the quasar images.

[3] Although based on the same data and method, these values are slightly different than obtained by Evans & Witt (2003) due different assumptions on the errors.

[4] Their expression misses the factor half in front of the summation.

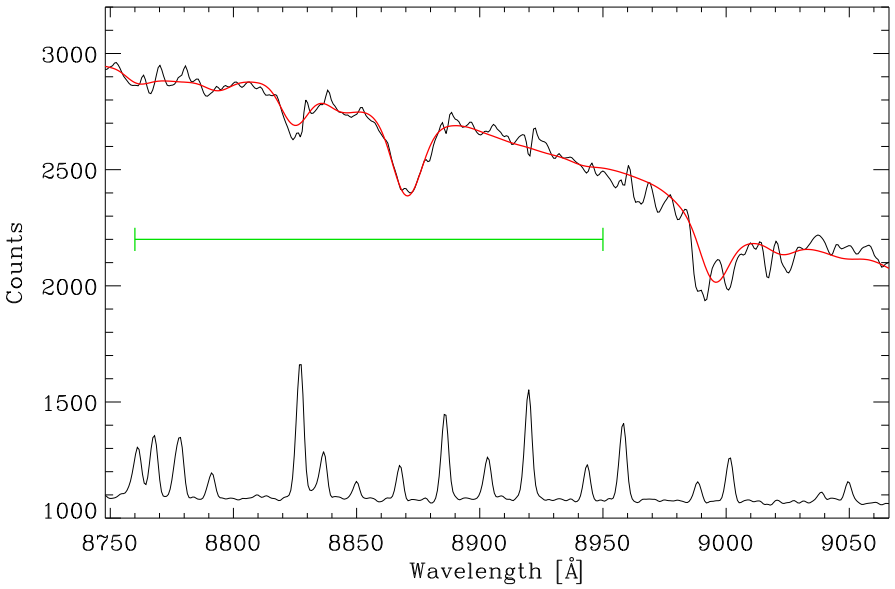

FIGURE 3 — *Spectrum from the center of the lens galaxy, showing the Ca II triplet region fitted by a composite of stellar population models. The sky spectrum is shown at the bottom. The horizontal bar indicates the region included in the fit to obtain the stellar kinematics.*

3.3 VELOCITY AND DISPERSION FIELDS

An accurate measurement of the mean line-of-sight velocities typically requires a signal-to-noise (S/N) ratio of 20 to match the stellar absorption lines in each spectrum. Stellar velocity dispersion measurements require higher S/N ratios to achieve the same accuracy. To measure reliable stellar kinematics we co-add the spectra using the adaptive spatial 2D-binning scheme of Cappellari & Copin (2003) to obtain in each resulting Voronoi bin a minimum S/N of $\sim$40, resulting in a total of 118 bins.

We measure the stellar kinematics of the lens galaxy using the penalized pixel-fitting algorithm of Cappellari & Emsellem (2004). We adopt the single stellar population (SSP) models of Vazdekis et al. (2003) as stellar templates. A non-negative linear combination of these templates is convolved with a Gaussian line-of-sight velocity distribution to obtain the mean line-of-sight velocity and velocity dispersion of each (binned) spectra in our merged datacube.

Fig. 3 shows the central spectrum of the lens galaxy with the best-fit SSP template (smooth line). We plot the typical sky spectrum below to indicate the regions where a possible bad sky subtraction has the strongest effect. This shows that an accurate sky subtraction is crucial given that many of the sky lines fall into the Ca II triplet absorption lines, and therefore affect our measurement of the mean line-of-sight velocity and velocity dispersion. This effect is of course stronger at larger radii in the lens galaxy, where the relative contribution from the sky is more significant.

The resulting stellar velocity V and dispersion σ fields are shown in Fig. 4, with superposed contours of the reconstructed image (obtained by collapsing the datacube in the spectral direction). The velocity field shows clear regular rotation around the projected minor axis of the bulge, with amplitude up to 100 km s^{-1}. Although the ve-

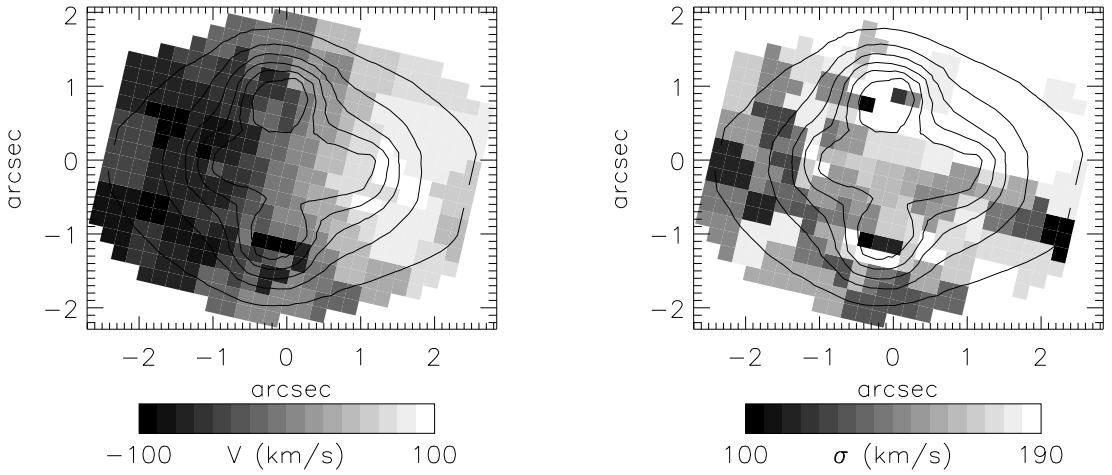

FIGURE 4 — *Mean velocity and velocity dispersion field of the lens galaxy in the Einstein Cross as measured from observations with the integral-field spectrograph GMOS on Gemini-North. The overlayed contours of the reconstructed image show the positions of the quasar images, which affect the kinematics only very locally. The velocity field shows clear and regular rotation around the (vertically aligned) short-axis of the bulge. The velocity dispersion is fairly constant across the field, except for the region towards the upper-right, where systematic effects cause the dispersion to be overestimated. (See p. 256 for a color version of this figure.)*

locity field is less well determined at the locations of the quasar images, most of their contribution has been efficiently removed during the extraction of the stellar kinematics. The dispersion field is more noisy, and is affected by systematics, in particular in the upper-right part. This is likely caused by the dominating sky lines in this region, which shift into the Ca II triplet absorption lines as a result of the corresponding positive mean velocity. The central dispersion measurements in between the quasar images, however, are robust around a value of $170\,\mathrm{km\,s^{-1}}$ (see § 5). We expect that a more detailed and careful treatment of the sky background will improve our stellar dispersion measurements, and we will investigate this in the near future. Because of the preliminary nature of the kinematic data, we limit the subsequent analysis to relatively simple axisymmetric dynamical models.

3.4 AXISYMMETRIC DYNAMICAL MODEL

For an axisymmetric model with a stellar distribution function that depends on only two integrals of motion $f = f(E, L_z)$, with E the energy and L_z the angular momentum component parallel to the symmetry z-axis, the second velocity moments are uniquely defined (e.g., Lynden-Bell 1962; Hunter 1977). They can be computed by solving the Jeans equations for a given potential and stellar density. For a given inclination i, we then obtain the line-of-sight projected second velocity moment $V_{\mathrm{RMS}} = \sqrt{V^2 + \sigma^2}$, which can be compared with the value obtained from the observed mean line-of-sight velocity V and velocity dispersion σ.

If the potential and density are described by an MGE-parametrization, the calculation of V_{RMS} reduces to a single one-dimensional integral via eqs (61–63) of Emsellem et al. (1994), with correction for a typographical error given in Cappellari et al. (2005).

i	$\log \Sigma_0$ ($M_\odot$ pc^{-2})	$\log \sigma'$ (arcsec)	q'
1	4.936	-1.779	0.670
2	4.971	-1.285	0.640
3	4.518	-0.915	0.650
4	4.145	-0.569	0.664
5	3.795	-0.230	0.663
6	3.460	0.105	0.667
7	3.133	0.445	0.667
8	2.836	0.814	0.665
9	2.623	1.376	0.670

TABLE 1 — *The parameters of the nine Gaussians in the MGE fit to the lens model of the Einstein Cross. The second column gives the central surface mass density (in $M_\odot$ pc^{-2}) of each Gaussian component, the third column the dispersion (in arcsec) along the major axis and the fourth column the observed flattening.*

i	$\log \mathrm{SB}_0$ ($L_\odot$ pc^{-2})	$\log \sigma'$ (arcsec)	q'
1	4.329	-3.601	0.700
2	3.935	-2.168	0.700
3	3.606	-1.444	0.700
4	3.293	-0.550	0.700
5	3.005	-0.098	0.700
6	2.845	0.530	0.700
7	2.261	1.352	0.700
8	2.160	2.111	0.414
9	1.334	2.613	0.700

TABLE 2 — *The parameters of the nine Gaussians in the MGE-fit to the HST/WFPC2/F814W I-band image of the surface brightness of the lens galaxy in the Einstein Cross. The second column gives the central surface brightness (in $L_\odot$ pc^{-2}) of each Gaussian component, the third column the dispersion (in arcsec) along the major axis and the fourth column the observed flattening.*

The MGE-parametrization of the lens potential follows from an MGE fit to the surface mass density $\Sigma(R', \theta')$ (3.5) of the lens model, shown by the dashed contours in Fig. 2 and with the corresponding parameters given in Table 1. Deprojection of this MGE fit provides the lens mass density from which the lens potential follows by solving Poisson's equation. As we saw in § 3.1, the stellar luminosity density $j_\star(R, \theta)$ follows from the MGE fit to the surface brightness with the corresponding parameters given in Table 2. With the potential and density known, the only free parameter left is the inclination, for which we assume the value of $i = 68°$, derived above from the ellipticity of the outer disk. When comparing the V_{RMS} predicted by the Jeans model with the observations, we also investigate a possible mass-scaling in the lens potential needed to better match the data.

Alternatively, we can build an axisymmetric Jeans model with the potential de-

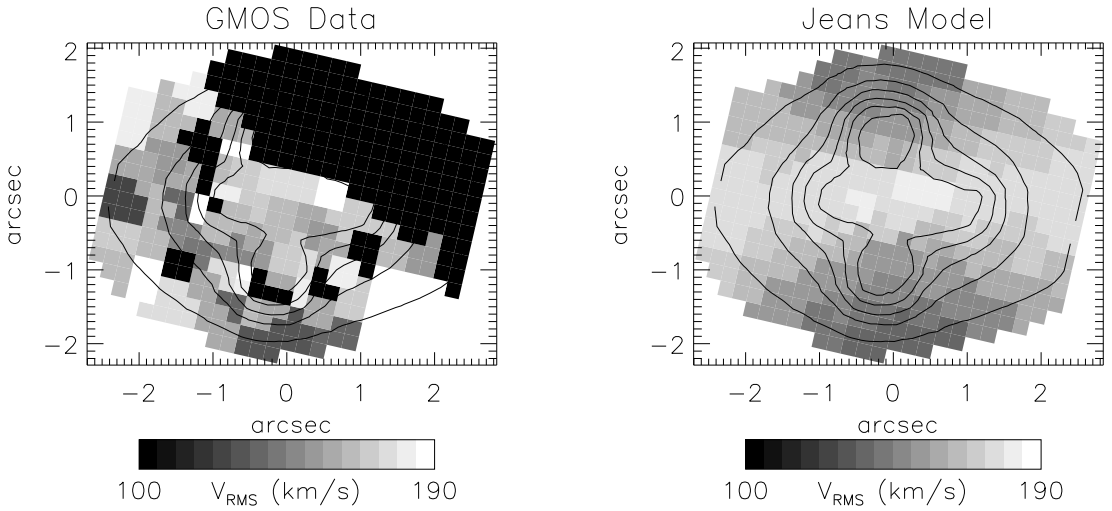

FIGURE 5 — *Two-integral axisymmetric Jeans model of the lens galaxy. Left panel: map of the second velocity moment as obtained from the observed velocity and dispersion field, where the region with systematic effects in the dispersion is excluded. Right panel: map of the second velocity moment from the best-fit Jeans model, based on the lens potential and the axisymmetric luminosity density inferred from the surface brightness.*

duced from the stellar luminosity density $j_\star(R,\theta)$ instead of using the lens potential. To this end we multiply $j_\star(R,\theta)$ with a constant mass-to-light ratio M/L to obtain the mass density, from which we then find the potential via Poisson's equation. In this case we have two free parameters, i and M/L. In what follows, we refer to these axisymmetric models as *stellar* Jeans models, whereas we call the above models, based on the lens potential, *lens* Jeans models.

4 RESULTS

In the left panel of Fig. 5, we show the second velocity moment $V_{\rm RMS}$ map, derived from the observed velocity and dispersion field (Fig. 4). We have excluded the region that is significantly affected by systematic effects in σ (see § 3.3), leaving 66 bins out of the total of 118 bins. The right panel shows $V_{\rm RMS}$ as predicted by a lens Jeans model [i.e., using the (scaled) potential from the lens model] at the measured inclination $i = 68°$. Across the relatively small field-of-view covered by the GMOS data, the predicted variation in $V_{\rm RMS}$ is small and of the order of the measurement uncertainties, so that there is only a weak indication for the 'butterfly' shape in the data. However, the central measurements are robust and can be used to reliably set the scaling.

We consider the region within the quasar images by selecting all bins within a radius that is half of the image separation of $1.8''$, i.e., all bins within the Einstein radius $R_E = 0.90''$. We find that the predictions of the *lens* Jeans model provide an acceptable fit to the resulting 15 dispersion measurements, although the best fit is obtained if the lens potential of the Jeans model is scaled by a factor 1.10. The best-fit *stellar* Jeans model predicts a similar butterfly shape for the projected second velocity moment. In this case the potential is inferred from the surface brightness, assuming a constant mass-to-light ratio to convert from light to mass (§ 3.4). We obtain a best-fit

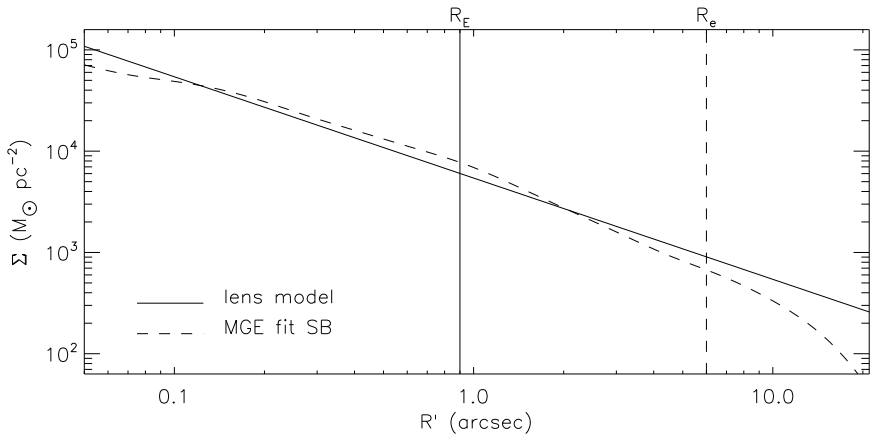

FIGURE 6 — *The surface mass density profile along the major axis of the lens galaxy. The solid line is the assumed power-law slope of the lens model. The dashed line shows the profile of the MGE fit to the I-band surface brightness. The solid and dashed vertical lines indicate respectively the Einstein radius $R_E = 0.90''$ and the effective radius $R_e \sim 6''$, obtained by fitting a $R^{1/4}$ profile to the I-band photometry in the inner 3″ bulge region.*

I-band mass-to-light ratio of $M/L = 3.6\,\mathrm{M}_\odot/\mathrm{L}_\odot$.

We compare the above best-fits by calculating the mass within the region enclosed by the critical curve $R_{\rm crit}$ given by eq. (3.5). This critical mass is nearly identical to the mass within the Einstein radius, which is the region of the dispersion field to which we fitted the Jeans models. For the best-fit lens Jeans model we obtain a mass of $\sim 1.76\times10^{10}\,\mathrm{M}_\odot$. After multiplying the MGE surface brightness model with the best-fit M/L, we find for the best-fit stellar Jeans model a very similar mass of $\sim 1.75\times10^{10}\,\mathrm{M}_\odot$. This does not mean that no dark matter is present in this region, as in both cases they are *total* masses (and *total* M/L), which in addition to the stellar mass may include a possible dark matter contribution.

At the same time, it is remarkable how similar the independent MGE fits of the surface mass density of the lens model (Fig. 2) and of the surface brightness (Fig. 1) are, and hence also their associated potentials. Both the orientation and the flattening (see fourth column of Tables 1 and 2) are comparable, suggesting that the shape of the total and stellar mass distributions are closely related. The radial profiles, shown in Fig. 6, cannot be compared in a similar way, since we assumed the power-law profile for the lens model as it is only weakly constrained by the lensing geometry. The critical mass, however, is not affected by our assumption of the power-law profile for the lens model, because it is almost independent of the lens model (e.g., Kochanek 1991; Evans & Witt 2001). The profile of the stellar dispersion can provide these constraints (e.g., Treu & Koopmans 2004). Unfortunately, due to the limited radial coverage, but mainly due to measurement uncertainties, this is not possible with the current preliminary velocity and dispersion field (but see § 6 below).

We can also compute the critical mass directly from the lens model via eq. (3.7). We find a mass of $\sim 1.62\times10^{10}\,\mathrm{M}_\odot$, which is about 8% lower than the critical masses from the best-fit lens and stellar Jeans model, but within the measurement uncertainties. Errors of a few per cent are typically assigned to critical mass measurements directly

from the lens model, although Ferreras, Saha & Williams (2005) found errors up to 10% by considering a large ensemble of possible lens models. Still, the errors in the critical masses from the Jeans models are expected to dominate. By comparing M/L determinations from Jeans models with those from three-integral Schwarzschild models fitted to high-quality integral-field kinematics, Cappellari et al. (2005) found as a realistic lower limit on the uncertainty in these determinations a value of 6%. The 15 dispersion measurements within $R_E = 0.90''$ have a mean value of $167\,\mathrm{km\,s^{-1}}$, with corresponding RMS value of $10\,\mathrm{km\,s^{-1}}$, i.e., on average a 6% error, which translates into an error of about 12% in mass. Hence, we estimate a typical error of 13% in the crititcal mass estimates from the Jeans models. This shows that the difference in the critical mass determinations from the lens model and from Jeans models is within the expected uncertainties.

We now add the $V_{\rm RMS}$ measurements outside R_E, but still excluding the systematically affected upper-right region (left panel of Fig. 4). When we fit these 66 dispersion measurements with the lens and stellar Jeans models, we find again very similar values for the critical masses, but about 10% higher than before and nearly 20% higher than the critical mass directly from the lens model. The mean velocity dispersion of $166\,\mathrm{km\,s^{-1}}$ is nearly identical to that of the 15 central measurements. The corresponding RMS value increases to $15\,\mathrm{km\,s^{-1}}$, resulting in an error on the mass of almost 20%. Although the difference between the various critical mass estimates is within the estimated uncertainties, we expect that the critical mass from the Jeans models is overestimated, mainly due to remaining systematics in the data, but also the model assumptions can have an effect (see the discussion below).

5 DISCUSSION

We find a central stellar velocity dispersion of $167 \pm 10\,\mathrm{km\,s^{-1}}$, based on 15 measurements within the Einstein radius $R_E = 0.90''$. The only other direct (single) measurement of the stellar dispersion is $215 \pm 30\,\mathrm{km\,s^{-1}}$ by Foltz et al. (1992). For a singular isothermal sphere lens model, we can use the relation $\Delta\theta = 8\pi(\sigma_{\rm SIS}/c)^2 D_{ls}/D_s$ (e.g., Kochanek 2000) with a separation $\Delta\theta \sim 1.8''$ of the four quasar images, to obtain a simple estimate for the dispersion of $\sigma_{\rm SIS} \sim 180\,\mathrm{km\,s^{-1}}$. Taking into account aperture correction and a range in velocity anisotropy, van de Ven, van Dokkum & Franx (2003) converted this to a central stellar dispersion of $168 \pm 17\,\mathrm{km\,s^{-1}}$. The King and de Vaucouleurs models of Kent & Falco (1988) predict a similar value of $\sim 166\,\mathrm{km\,s^{-1}}$, and also Barnes et al. (1999) find a value of $165 \pm 23\,\mathrm{km\,s^{-1}}$ based on their two H I rotation curve measurements. All these measurements are lower than that of Foltz et al. (1992), but in perfect agreement with ours. Their optical long-slit measurement might be affected by the very bright quasar images, whereas our measurements are in the less-affected Ca II triplet region and are spatially resolved, allowing for a clean separation of the quasar images.

A large variety of different lens models have been constructed for the Einstein Cross, most of which fit the positions of the quasar images but not their relative flux ratios. Although they predict significantly different flux ratios, the mass M_E within the Einstein radius $R_E = 0.90''$ is expected to be similar, because, as mentioned before, it is insensitive to the details of the lens model. In Table 3, we compare measurements of M_E from our analysis with values obtained from the literature, taking into account the inverse scaling with the Hubble constant. The difference between the circular

reference	M_E ($10^{10}\,\mathrm{M}_\odot$)
scale-free $\beta = 1$ lens model	1.60
best-fit lens Jeans model	1.74
best-fit stellar Jeans model	1.73
Rix, Schneider & Bahcall (1992)	1.52
Wambsganss & Paczýnski (1994)	1.56
Chae, Turnshek & Kehersonsky (1998)	1.58
Schmidt, Webster & Lewis (1998)	1.58
Trott & Webster (2002)	1.54
Ferreras, Saha & Williams (2005)	1.87

TABLE 3 — *Measurements of the Einstein mass M_E, i.e., the projected mass within the Einstein radius, for the Einstein Cross. The first four measurements follow from our analysis, the remaining are taken from the literature, taking into account an inverse scaling with the Hubble constant, for which we assume $H_0 = 71\,\mathrm{km\,s^{-1}\,Mpc^{-1}}$.*

area within R_E and the non-circular critical area causes a 1% decrease in M_E with respect to critical mass measurements we obtained in § 4. Given the typical error of a few per cent in the determination of M_E from the lens models, we conclude that the measurement from our lens model, that does fit the (radio) flux ratios, is consistent with all previous measurements. The one exception is the determination by Ferreras et al. (2005), who find a value higher than all others.

Although our two M_E values from the Jeans models fitted to the GMOS data are on average somewhat higher, they are safely within the uncertainties, given the estimated 13% error on these mass determinations. Part of the offset might be the result of our model assumptions of axisymmetry and two-integral distribution functions. Although the bar is clearly visible in the large-scale V-band image in Fig. 1, its effect in the inner bulge-dominated region is minimal, with an estimated mass contribution of only 5 per cent (Schmidt, Webster & Lewis 1998). This is supported by the observed velocity field, which shows regular rotation around the minor axis of the bulge. The two-integral assumption implies velocity isotropy in the meridional plane, which can have a direct effect on the mass estimate. Nevertheless, Cappellari et al. (2005) found that M/L determinations from axisymmetric two-integral Jeans models seem to be consistent with those obtained from three-integral Schwarzschild models. The latter models have full freedom in velocity anisotropy, but consequently more extensive and accurate kinematic observational constraints are required. When we use the $(M/L) - \sigma$ relation derived by these authors from Schwarzschild models, we find for our measured central dispersion of $167\,\mathrm{km\,s^{-1}}$ a predicted I-band $M/L \sim 3.3\,\mathrm{M}_\odot/\mathrm{L}_\odot$. This is just 10% lower than we found from our stellar Jeans model, and implies a critical mass of $\sim 1.6 \times 10^{10}\,\mathrm{M}_\odot$, equal to that measured directly from the lens model.

6 CONCLUSIONS

We have studied the total mass distribution in the inner parts of the lens galaxy in the Einstein Cross by fitting axisymmetric models based on an accurate lens model and a realistic luminosity density to spatially resolved kinematics obtained via observations with the integral-field spectrograph GMOS. We have found that the stellar velocity dispersion measurements have an average value of $167 \pm 10\,\mathrm{km\,s^{-1}}$ within the

Einstein radius $R_E = 0.90''$, and are in agreement with previous predictions from lens models. The constructed scale-free lens model fits the positions as well as relative (radio) fluxes of the quasar images, and provides an Einstein mass $M_E = 1.60 \times 10^{10}\,\mathrm{M}_\odot$ consistent with previous measurements.

We have obtained the luminosity density by deprojection of the surface brightness, and used it to construct axisymmetric two-integral Jeans models, which we fitted to the two-dimensional kinematic observations. Using the potential inferred from the lens model or from the luminosity density for a constant mass-to-light ratio M/L, we have found that in both cases the Einstein mass of the best-fit Jeans model is consistent with that of the lens model within the measurement uncertainties. The best-fit I-band $M/L = 3.6\,\mathrm{M}_\odot/\mathrm{L}_\odot$ is consistent with the prediction from the $M/L - \sigma$ relation of Cappellari et al. (2005). Moreover, we have found that the M_E values from both best-fit Jeans models are the same within 1% and that the shape of the density inferred from the lens model and from the surface brightness is similar, suggesting that mass and light are similarly distributed. However, further analysis of the kinematic data, with in particular a more careful treatment of the sky background, is needed to also establish the radial profile of the mass distribution, before firm conclusions on the total mass distribution can be drawn.

Our preliminary study has shown that with integral-field spectrographs like GMOS it is possible, although very challenging, to obtain reliable spatially resolved kinematics of the lens galaxies in nearby gravitational lens systems, allowing for the unique combination of lensing and stellar dynamics to constrain the mass distribution. An even better candidate than the Einstein Cross for this kind of study is the newly-discovered gravitational lens system ESO325+G004 (Smith et al. 2005). The system is closer ($z = 0.0345$), the possible contamination from the faint quasar images is expected to be minimal, and above all, the lens galaxy is a bright giant elliptical galaxy. Hence, it becomes even feasible to measure absorption line strengths to obtain an independent estimate of the stellar mass-to-light ratio from the stellar population analysis. By improving our kinematic data on the Einstein Cross, as well as by obtaining integral-field spectroscopic observations on objects such as ESO325+G004, we expect to place constraints on the dark matter distribution in the inner parts a early-type galaxies, without being limited by ad-hoc assumptions on the geometry or velocity anisotropy.

ACKNOWLEDGMENTS

We are grateful to Jean-Rene and Matt Mountain for granting us director's discretionary time for this project and Tracy Beck for efficient and cheerful support.

REFERENCES

Agol E., Jones B., Blaes O., 2000, ApJ, 545, 657
Barnes D. G., Webster R. L., Schmidt R. W., Hughes A., 1999, MNRAS, 309, 641
Bennett C. L., et al. 2003, ApJS, 148, 1
Binney J., Merrifield M., 1998, Galactic astronomy. Princeton, NJ, Princeton University Press
Blanton M., Turner E. L., Wambsganss J., 1998, MNRAS, 298, 1223
Cappellari M., 2002, MNRAS, 333, 400
Cappellari M., Copin Y., 2003, MNRAS, 342, 345
Cappellari M., Emsellem E., 2004, PASP, 116, 138
Cappellari M., et al 2005, MNRAS, submitted, astro-ph/0505042

Carollo C. M., de Zeeuw P. T., van der Marel R. P., Danziger I. J., Qian E. E., 1995, ApJ, 441, 25
Dai X., Chartas G., Agol E., Bautz M. W., Garmire G. P., 2003, ApJ, 589, 100
Dejonghe H., 1987, MNRAS, 224, 13
Dolphin A. E., 2000, PASP, 112, 1397
Emsellem E., Monnet G., Bacon R., 1994, A&A, 285, 723
Evans N. W., Witt H. J., 2001, MNRAS, 327, 1260
Evans N. W., Witt H. J., 2003, MNRAS, 345, 1351
Falco E. E., Lehar J., Perley R. A., Wambsganss J., Gorenstein M. V., 1996, AJ, 112, 897
Ferreras I., Saha P., Williams L. L. R., 2005, ApJ, 623, L5
Fitte C., Adam G., 1994, A&A, 282, 11
Foltz C. B., Hewett P. C., Webster R. L., Lewis G. F., 1992, ApJ, 386, L43
Gerhard O., Kronawitter A., Saglia R. P., Bender R., 2001, AJ, 121, 1936
Gerhard O. E., 1993, MNRAS, 265, 213
Hook I. M., Jørgensen I., Allington-Smith J. R., Davies R. L., Metcalfe N., Murowinski R. G., Crampton D., 2004, PASP, 116, 425
Huchra J., Gorenstein M., Kent S., Shapiro I., Smith G., Horine E., Perley R., 1985, AJ, 90, 691
Hunter C., 1977, AJ, 82, 271
Irwin M. J., Webster R. L., Hewett P. C., Corrigan R. T., Jedrzejewski R. I., 1989, AJ, 98, 1989
Jing Y. P., Suto Y., 2002, ApJ, 574, 538
Kauffmann G., van den Bosch F., 2002, Scientific American, 286, 36
Kent S. M., Falco E. E., 1988, AJ, 96, 1570
Kochanek C. S., 1991, ApJ, 373, 354
Koopmans L. V. E., Treu T., 2003, ApJ, 583, 606
Lambas D. G., Maddox S. J., Loveday J., 1992, MNRAS, 258, 404
Lynden-Bell D., 1962, MNRAS, 123, 447
Mediavilla E., Arribas S., del Burgo C., Oscoz A., Serra-Ricart M., Alcalde D., Falco E. E., Goicoechea L. J., Garcia-Lorenzo B., Buitrago J., 1998, ApJ, 503, L27
Metcalf R. B., Moustakas L. A., Bunker A. J., Parry I. R., 2004, ApJ, 607, 43
Monnet G., Bacon R., Emsellem E., 1992, A&A, 253, 366
Murray G. J., Allington-Smith J. R., Content R., Davies R. L., Dodsworth G. N., Miller B., Jorgensen I., Hook I., Crampton D., Murowinski R. G., 2003, SPIE, 4841, 1750
Navarro J. F., Frenk C. S., White S. D. M., 1997, ApJ, 490, 493
Oguri M., Keeton C. R., 2004, ApJ, 610, 663
Primack J. R., 2004, in IAU Symp. 220: Dark Matter in Galaxies, eds. S. D. Ryder, D. J. Pisano, M. A. Walker, and K. C. Freeman, p. 53
Racine R., 1991, AJ, 102, 454
Rix H.-W., de Zeeuw P. T., Cretton N., van der Marel R. P., Carollo C. M., 1997, ApJ, 488, 702
Romanowsky A. J., Douglas N. G., Arnaboldi M., Kuijken K., Merrifield M. R., Napolitano N. R., Capaccioli M., Freeman K. C., 2003, Science, 301, 1696
Schlegel D. J., Finkbeiner D. P., Davis M., 1998, ApJ, 500, 525
Schmidt R., Webster R. L., Lewis G. F., 1998, MNRAS, 295, 488
Schneider P., Ehlers J., Falco E. E., 1992, Gravitational Lenses. Springer-Verlag Berlin Heidelberg New York
Smith R. J., Blakeslee J. P., Lucey J. R., Tonry J., 2005, ApJ, 625, L103
Treu T., Koopmans L. V. E., 2004, ApJ, 611, 739
Trott C. M., Webster R. L., 2002, MNRAS, 334, 621
van Albada T. S., Bahcall J. N., Begeman K., Sancisi R., 1985, ApJ, 295, 305
van de Ven G., van Dokkum P. G., Franx M., 2003, MNRAS, 344, 924 (Chapter 7)
van der Marel R. P., 1991, MNRAS, 253, 710
van der Marel R. P., Franx M., 1993, ApJ, 407, 525
van Dokkum P. G., 2001, PASP, 113, 1420
Vazdekis A., Cenarro A. J., Gorgas J., Cardiel N., Peletier R. F., 2003, MNRAS, 340, 1317
Yee H. K. C., 1988, AJ, 95, 1331